Three-dimensional crystal growth—II: nonlinear simulation and control of the Mullins–Sekerka instability

Vittorio Cristini[a,b], John Lowengrub[b,*]

[a] *Department of Biomedical Engineering, 200 Rockwell Engineering Center, USA*
[b] *Department of Mathematics, University of California at Irvine, Irvine CA 92697-2715, USA*

Abstract

In this paper, Part II of our study, we extend our previous analysis (J Crystal Growth 240 (2002) 267) of the linear evolution of non-spherical growing crystals in three dimensions into the nonlinear regime characterized by large shape perturbations. We focus on a solid crystal growing in an undercooled liquid with isotropic surface tension and interface kinetics. We use a new, adaptive boundary integral method to simulate the morphological evolution of the growing crystals. Our simulations reveal that when the far-field heat flux into the system is prescribed by appropriately varying the undercooling in the far field, the Mullins–Sekerka instability that would arise under constant undercooling can be suppressed. In particular, we demonstrate that there exist critical conditions of flux at which self-similar or nearly self-similar nonlinear evolution occurs and the shape is dominated by a given mode leading to non-spherical, nearly shape invariant growing crystals. This result was predicted by our previous analysis (see Ref. Cristini and Lowengrub) and suggests that our theory is applicable to real physical systems. We provide a simulation of a physical experiment that might be able to be carried out in a laboratory in which a desired shape of a crystal is achieved and maintained during growth by appropriately prescribing the far-field heat flux.
© 2004 Published by Elsevier B.V.

1. Introduction

The growth of a single crystal from an under-cooled melt is a fundamental problem in materials science. When the temperature of the melt is held

constant in time (below the phase change temperature), a growing spherical crystal undergoes the Mullins–Sekerka instability and becomes unstable to perturbations with successively smaller wavelengths [1,2]. This results in highly complex shapes (e.g. snowflakes). Mullins and Sekerka [2] first identified the possibility of growing crystals with compact, stable shapes in situations where there are a number of crystals present that act to

*Corresponding author. Fax: +1-612-626-2017.
E-mail addresses: cristini@math.uci.edu (V. Cristini),
lowengrb@math.uci.edu (J. Lowengrub).

reduce the effective undercooling of an individual crystallite. Mullins and Sekerka did not quantify this idea further, however.

In part I of our study, we reformulated the linear theory developed by Mullins and Sekerka, and later by Coriell and Parker [3,4] who included the effect of interface kinetics. We quantified the idea that Mullins–Sekerka instability can be suppressed by controlling the far-field heat flux into the system. In particular, there is a critical flux J_l, which is a monotonically increasing function of each perturbation wavenumber l, such that during growth of a perturbed crystal under a prescribed heat flux J, only those perturbations with wavenumbers l such that $J_l < J$ grow unstable. In contrast to the case in which the far-field temperature is held constant, if J is constant only a finite number of perturbations may be unstable throughout growth. Thus, if the flux J is small enough, the crystal will grow with a stable compact shape. In addition, if $J = J_l$ and the perturbation contains a single wavenumber l then the perturbed crystal will evolve self-similarly (i.e. shape invariant).

In part I, we exploited the relationship between the far-field heat flux J and the undercooling in the far field ΔT^∞, to give an explicit prescription of how the far-field temperature should be varied in time to maintain constant flux conditions without requiring feedback from the local crystal environment. In particular, we obtained $\Delta T^\infty \sim -J^{2/3} t^{-1/3}$ where J and ΔT^∞ have been appropriately non-dimensionalized (we note this scaling was previously obtained and explained in Ref. [5]). It is intriguing that time scaling with exponent $-1/3$ occurs naturally in many systems undergoing coarsening in adiabatic conditions (e.g. see the review [6]). Moreover, experiments have shown that during coarsening in pure materials under heat diffusion and in two-phase alloy mushy zones under solute diffusion control, the coarsening crystals attain compact, stable shapes (e.g. see Refs. [7–9]). Further work needs to be done to understand whether these results provide indirect experimental evidence for our theory.

In this paper, Part II of our study, we extend our previous analysis of the linear evolution of growing crystals in three dimensions into the nonlinear regime. We focus on a solid crystal growing in an undercooled liquid with isotropic surface tension and interface kinetics. We use a new, adaptive boundary integral method to simulate the morphological evolution of the growing crystals. This method differs in several important ways from that we recently presented in Ref. [10] in the context of diffusional evolution of microstructure in two-phase, elastically inhomogeneous systems. Ref. [10] is, to the best of our knowledge, the first work in which a boundary integral method is used to simulate evolving precipitate shapes in three dimensions. Previously, boundary integral methods have been used to determine equilibrium precipitate shapes in the context of elastic media by minimizing the system energy (e.g. see Refs. [11–13]). Simulations of three-dimensional growing crystals have been performed using primarily phase-field methods (e.g. see the recent reviews [14,15]), sharp interface adaptive finite element methods (e.g. see Ref. [16]) and more recently, level-set methods [17].

Here, we use a novel time and space rescaling of the equations, together with a more efficient numerical implementation of the boundary integral equations, that allow us to accurately simulate crystal evolution for much longer times (and hence larger crystal sizes) than has been possible previously.

Our simulations in the nonlinear regime confirm the existence of critical fluxes for suppression of the Mullins–Sekerka instability and nearly self-similar growth of crystals. The control of the shape is robust to shape perturbations and nonlinearity as unstable growth is highly impeded by nonlinear diffusional interactions among wavenumbers. This suggests that our theory is applicable to real physical systems to effectively control the shape of growing crystals. Accordingly, we provide a simulation of a physical experiment that could be carried out in the laboratory in which a desired shape of a crystal is achieved and maintained during growth by appropriately prescribing the far-field heat flux.

The paper is organized as follows. In Section 2, we review the physical scales and non-dimensionalization and the linear analysis of perturbed crystals. In Section 3, we present a new, boundary

integral formulation and its implementation on an adaptive computational mesh. In Section 4, we present numerical results and comparisons to theory. In Section 5, we give a discussion of the work and future directions.

2. The theory

2.1. Physical scales, non-dimensional parameters and formulation

Assuming that the crystal evolution is quasi-steady (i.e. diffusion occurs very rapidly and is governed by Laplace's equation), the relevant time scales for the growth of a solid crystal from a liquid melt are [1]: The surface tension time τ_γ, the kinetic attachment time[1] τ_μ and the growth time due to the driving force which is determined by either an undercooling in the far-field resulting in the time scale τ_∞ or by a far field heat flux resulting in the time scale τ_J. Let R_0 denote the initial equivalent radius of the crystal (i.e. radius of a sphere with the same volume) and let J_0 be the initial value of the flux, then the time scales are given by

$$\tau_\gamma = \frac{R_0^2}{K_2 \Delta T_\gamma}, \quad \tau_\mu = \frac{R_0}{\mu \, \Delta T_\gamma}, \quad \tau_\infty = \frac{R_0^2}{K_2 \, \Delta T_0^\infty}, \quad \tau_J = \frac{R_0^d}{J_0}, \tag{1}$$

where $K_2 = k_2/L$ and k_2 is the heat conductivity in the liquid phase (herein 1 and 2 denote the solid and liquid phases, respectively), L is the latent heat per unit volume (the density is taken to be uniform and equal in the two phases), $\Delta T_\gamma = \gamma T_{PH}/(LR_0)$ is the characteristic decrease in the phase change temperature associated with a curved interface (compared to a flat interface), γ is the (isotropic) surface tension and T_{PH} is the phase change temperature for a flat interface. Further, μ is the (linear) kinetic coefficient, $\Delta T_0^\infty = T_{PH} - T_0^\infty$ is the initial undercooling and T_0^∞ is the initial far-field temperature, $d = 2,3$ is the space

dimension and the initial heat flux $J_0 = \lim_{R\to\infty} \frac{1}{4\pi} \int_{S_R} K_2 \nabla T \bullet \mathbf{n} \, dS$, where S_R is a sphere of radius R containing the initial crystal.

When the undercooling is a constant independent of the crystal size R_0, the Mullins–Sekerka instability occurs in which a growing sphere is linearly unstable to successively shorter wavelength perturbations [2]. This can be seen via the ratio of the growth and surface tension relaxation time scales: $\tau_\infty/\tau_\gamma \propto R_0^{-1}$. Thus, when R_0 is large, the surface tension has less time to act to smooth the shape than when R_0 is small.

In contrast, when the heat flux is held constant, the relevant ratio of relaxation and growth time scales is: $\tau_J/\tau_\gamma \propto R_0^{d-3}$. Consequently, when the dimension $d = 3$, the relaxation and growth time scales balance and the Mullins–Sekerka instability can be suppressed.

When $d=2$, the growth and relaxation time scales balance only if the flux $J_0 \propto R_0^{-1}$. Very recently, we have performed nonlinear analysis and simulations in 2D and found that varying the far-field heat flux in this manner indeed suppresses the Mullins–Sekerka instability and makes self-similar evolution possible in the nonlinear regime [18].

Equating the growth time scales τ_J and τ_∞ gives the relation

$$J_0 = R_0^{d-2} K_2 \, \Delta T_0^\infty \tag{2}$$

between the far-field heat flux and undercooling. So, when J_0 is constant and $d = 3$, the relative magnitude of the flux and undercooling scales with the characteristic size of the system R_0. This relationship will be exploited later to vary the undercooling in order to achieve a desired flux.

We next define three dimensionless parameters [1] the (isotropic) kinetic coefficient ε, the ratio of conductivities k and the capillary number[2] Ca that rescales flux:

$$\varepsilon = \tau_\mu/\tau_\gamma, \ k = k_1/k_2, \ Ca = \tau_\gamma/\tau_J, \tag{3}$$

[1] We assume here a linear kinetic relation between the deviation from the phase-change temperature at equilibrium and the normal velocity of the interface. For simplicity, we consider isotropic kinetics unless stated otherwise.

[2] We use the term capillary number because of the analogy with multiphase flow where this number relates the ratio of the viscous deformation force to the stabilizing surface tension force.

The physical variables are non-dimensionalized by [1]

$$t' = t/\tau_\gamma, \ \mathbf{x}' = \mathbf{x}/R_0, \ T' = \frac{T - T_{PH}}{\Delta T_\gamma},$$ (4)

The nondimensional flux is given by

$$J' = Ca \frac{J}{J_0}.$$ (5)

Hereafter, we drop the primes denoting the dimensionless variables. The non-dimensional system of equations governing the evolution are given by

$$\nabla^2 T_i = 0 \ \text{in} \ \Omega_i, \quad i = 1, 2,$$ (6)

$$(T_1)_\Sigma = (T_2)_\Sigma = -\kappa - \varepsilon V,$$ (7)

$$V = \mathbf{n} \bullet (k\nabla T_1 - \nabla T_2),$$ (8)

$$\begin{cases} J = (4\pi)^{-1} \int_\Sigma V \ d\Sigma, \ \text{or,} \\ \lim_{|x| \to \infty} T_2(\mathbf{x}, t) = T_\infty \end{cases}$$ (9)

where κ is the total curvature ($\kappa = 2$ on the unit sphere), $\mathbf{n}$ is the normal vector on the solid/liquid interface $\Sigma = \partial\Omega_1$ directed in the liquid phase Ω_2, and V is the normal velocity of Σ.

2.2. Review of linear theory: the relation between flux and undercooling

Here, we focus primarily on constant flux conditions. The linear theory, under these conditions, was recently developed [1]. The results for constant temperature can be found in Refs. [1–4]. We consider the linearized evolution of a sphere of radius R perturbed by a spherical harmonic $Y_{l,m}$:

$$r_\Sigma(\theta, \phi, t) = R(t) + \delta_{l,m}(t) Y_{l,m}(\theta, \phi),$$ (10)

where θ is the polar angle (measured from $\mathbf{z}$ to $\mathbf{r}$) and ϕ is the azimuthal angle (measured from $\mathbf{x}$ to the projection of $\mathbf{r}$ in the x–y plane)[3]. The flux and far-field temperature are related by

$$J = \frac{-1}{1 + \varepsilon/R}(T^\infty R + 2),$$ (11)

to within an $O(\delta_{l,m}^2/R)$ error. When the far-field flux J is constant, the far-field temperature $T^\infty \sim -1/R$, for large R, as predicted by the scaling argument in the previous section. In constrast, when T^∞ is constant, then $J \sim R$ and the flux grows unboundedly as the crystal evolves thus leading to the Mullins–Sekerka instability.

The linear evolution of the perturbation $\delta_{l,m}(t)$, with respect to the underlying crystal size $R(t)$, and $\delta_{l,m}(0) = \delta_0$ and $R(0) = 1$, under constant flux conditions $J \neq 0$ is

$$\frac{\delta_{l,m}/\delta_0}{R} = R^{(l-2)(1-J_l/J)}$$

$$\left(\frac{1 + (1 + \bar{k}l)\varepsilon/R}{1 + (1 + \bar{k}l)\varepsilon}\right)^{1 + (l-1)(1-J_l/J)},$$ (12)

where the radius is given by

$$R = (1 + 3J \ t)^{1/3}$$ (13)

and the critical flux J_l is given by

$$J_l = \frac{(l + 2)(l - 1)(1 + \bar{k} \ l)}{l - 2}.$$ (14)

Note that here (and in [Ref. 1]) a critical flux is introduced instead of a critical radius as was used in Refs. [2–4] Note that the evolution of $\delta_{l,m}(t)$ does not depend on m. Further, if $\varepsilon = 0$ and $J = J_l$, Eq. (12) demonstrates that the growing crystal evolves self-similarly $\left(i.e. \ \frac{\delta_{l,m}/\delta_0}{R} = 1\right)$ in the linear regime. On the other hand, if $\varepsilon > 0$ and $J = J_l$, then

$$\lim_{t \to \infty} \frac{\delta_{l,m}/\delta_0}{R} = \left(1 + (1 + \bar{k}l)\varepsilon\right)^{-1}$$

and the evolution tends to become self-similar as the crystal grows. We note that if $\varepsilon > 0$, there is a non-constant critical flux $J_l = J_l(\varepsilon/R)$ such that the evolution is self-similar [1]. Moreover, from Eq. (12), we see that if $J > J_l$, the evolution is unstable and the perturbation grows unbounded although there is initial decay if $\varepsilon > 0$. If $J < J$, the evolution is stable and the perturbation decays to zero.

We also determine the harmonic with the fastest growth rate. This further characterizes growth as this harmonic should dominate the shape. There is a flux J_l^* that makes the lth spherical harmonic

---

[3] The vectors $\mathbf{x}$, $\mathbf{y}$, $\mathbf{z}$ denote the Cartesian coordinate directions; the vectors $\mathbf{r}$, θ, ϕ denote the spherical coordinate directions.

possess the largest growth rate [1]. This flux is given explicitly by

$$J_l^* = 1 + 2l + \bar{k}(3l^2 + 2l - 2) \tag{15}$$

in the limit $\varepsilon/R \to 0$. Note that $J_l^* > J_l$ for $l > 3$. Moreover, the dependence of J_l^* on ε/R is rather weak and so the limiting value approximates the values at finite values of ε/R quite well [1]. This result has several important consequences. First, only a finite number of harmonics ever have the fastest growth rate even with kinetics. Second, as a consequence, unstable growth is highly constrained in contrast to the case in which the far-field temperature T^∞ is constant. Third, by taking the flux $J = J_l^*$, we expect that we can control the shape during growth.

2.3. Example of an experimental system: self-similar growth of succinonitrile crystals

Let us now explore the implications of the theory for self-similar growth for a specific experimental system consisting of the organic liquid/solid succinonitrile (SCN). The material properties of liquid and solid SCN have been determined in Refs. [19] and are outlined in Table 1. This material has negligible interface kinetics and low surface tension anisotropy. The thermal conductivities of the solid and liquid phases very nearly match and there is a small density difference between the phases [19] (i.e. $(\rho_s - \rho_L)/\rho_s = 0.018$).

Let us first determine relevant time scales given in Eq. (1) and let the initial crystal size $R_0 = r_0 \, \mu m$

where r_0 is a non-dimensional number. We then find that $\Delta T_\gamma = 6.4 \times 10^{-2}/r_0$ K and $K_2 = 4.8 \times 10^3 \, \mu m^2/s$ K. Assuming that the flux is constant in time, we find

$$\tau_\gamma \approx 3.3 \times 10^{-3} \, r_0^3 \, s, \quad \tau_J \approx 3.3 \times 10^{-3} \, \frac{r_0^3}{J} \, s. \tag{16}$$

The dimensional undercooling $\Delta T^\infty(t)$ at the dimensional time t is obtained from Eq. (11). In terms of the dimensionless flux J, this yields

$$-\Delta T^\infty(t) = \Delta T_\gamma (J + 2)\left(1 + 3\frac{J}{\tau_\gamma} t\right)^{-1/3}$$
$$\approx \frac{6.4 \times 10^{-2}}{r_0}(J + 2)\left(1 + 10^3 \frac{J}{r_0^3} t\right)^{-1/3} \text{(K)} \tag{17}$$

Letting $r_0 \approx 10$ (which is plausible experimentally [20]) and $J \approx 10^2$ (which is consistent with mode $l = 4$ evolving self-similarly), we obtain $\tau_\gamma \approx 3.3 \, s$, $\tau_J \approx 3.3 \times 10^{-2}$ s and $-\Delta T^\infty(t) \approx 0.64(1 + 10^2 \, t)^{-1/3}$ K. The radius of the crystal is $R \approx 10 \, (1 + 10^2 t)^{1/3} \, \mu m$. Note that the time scale for diffusion is $\tau_D = R_0^2/D \approx 1 \times 10^{-3}$ s, where D is the diffusion constant in the liquid phase. Therefore, the quasi-steady assumption is still reasonable and becomes a better approximation as the crystal grows in size.

In Table 2, we present the time required, together with the final value of undercooling, to grow a crystal to a millimeter size under the constant flux conditions described above (i.e. shape-invariant conditions). Note that after a rapid initial transient, the radius increases quite slowly in time because of the $t^{1/3}$ scaling. We believe these results demonstrate that it is experimentally feasible to grow millimeter-sized succinonitrile crystals with controlled shapes.

Table 1
Materials properties of succinonitrile (from Ref. [19]).

Properties	Value
Interfacial tension	8.95×10^{-15} J/μm^2
Surface energy anisotropy (4-fold)	0.005
Latent heat	4.627×10^{-11} J/μm^3
Diffusivity (solid)	$1.14 \times 10^5 \, \mu m^2/s$
Diffusivity (liquid)	$1.16 \times 10^5 \, \mu m^2/s$
Conductivity (solid)	2.24×10^{-7} J/μm s K
Conductivity (liquid)	2.22×10^{-7} J/μm s K
Phase change temperature	331.24 K

Table 2
Results of theory for growth of compact, succinonitrile crystals

Desired radius of crystal(mm)	Growth time required	Final undercooling(K)
0.1	10 s	−0.29
1.0	2.8 h	−0.14
10.0	115 days	−0.064

3. Numerical methodology

3.1. Boundary integral formulation

In the special case $k = 1$ (*i.e.* matched thermal diffusivities) considered herein, the temperature-field T in both domains Ω_1 and Ω_2 can be represented using a single-layer potential in which the potential is the normal velocity $V = \mathbf{n} \bullet d\mathbf{x}/dt$ [21,22], i.e.

$$T(\mathbf{x}) = \int_{\Sigma} V(\mathbf{y}) G(\mathbf{x} - \mathbf{y}) \, d\Sigma(\mathbf{y}), \tag{18}$$

where $G(\mathbf{x}) = 1/4\pi|\mathbf{x}|$ is the Green's function. When the kinetic coefficient $\varepsilon > 0$ (finite kinetics), Eqs. (6)–(9) can then be recast into a 2nd kind Fredholm integral equation[4] at the interface $\Sigma(t)$

$$\int_{\Sigma} V(\mathbf{y}) G(\mathbf{x} - \mathbf{y}) \, d\Sigma(\mathbf{y}) + \varepsilon V(\mathbf{x}) + T^{\infty} = -\kappa(\mathbf{x}), \tag{19}$$

$$\frac{1}{4\pi} \int_{\Sigma} V(\mathbf{y}) \, d\Sigma(\mathbf{y}) = J \tag{20}$$

For a given interface Σ and flux J, these equations determine uniquely the normal velocity V and T^{∞}. We also further rescale space and time in order to separate the bulk growth dynamics from the shape evolution. This allows us to compute the solutions to the governing equations accurately for very long times by (i) evolving the equations on a time scale such that the effective crystal radius increases exponentially in the new time variable, (ii) obtaining more accurate discretizations since the bulk growth is solved either exactly (constant flux conditions) or very accurately through an ordinary differential equation (constant far-field temperature conditions) and (iii) using an adaptive surface mesh to resolve only the evolving crystal morphology and not the bulk growth.

The temporal and spatial rescaling is as follows. Let $\overline{\mathbf{x}}$ and $\overline{t}$ be the new space and time variables

---

[4]Note that if the interface kinetics $\varepsilon = 0$, then the equation becomes a first-kind Fredholm integral equation. For this case, we have developed an alternative approach using a dipole layer representation (L. Pham, J. Lowengrub, Q. Nie, V. Cristini, J. Comp. Phys., in preparation).

---

defined by

$$\mathbf{x} = \bar{R}(\bar{t}) \, \overline{\mathbf{x}}, \quad \bar{t} = \int_{0}^{t} \frac{dt'}{R(t')^3}, \tag{21}$$

where $\bar{R}(\bar{t}) = R(t(\bar{t}))$ is chosen such that the crystal volume in the new frame is constant in time. As we see below, this choice of $\bar{R}$ is consistent with the result of linear theory given in Section 2B. The normal velocity in the new frame $\bar{V} = \mathbf{n} \bullet d\overline{\mathbf{x}}/dt$ then satisfies

$$\int_{\bar{\Sigma}} \bar{V}(\overline{\mathbf{y}}) \, d\bar{\Sigma}(\overline{\mathbf{y}}) = 0. \tag{22}$$

With this change of variables, Eqs. (19)–(20) are equivalent to the Fredholm integral equation

$$\int_{\bar{\Sigma}} \bar{V}(\overline{\mathbf{y}}) G(\overline{\mathbf{x}} - \overline{\mathbf{y}}) \, d\bar{\Sigma}(\overline{\mathbf{y}}) + \frac{\varepsilon}{R} \bar{V}(\overline{\mathbf{x}}) + \bar{T}^{\infty}$$
$$= -\bar{\kappa}(\overline{\mathbf{x}}) - \bar{R}^{-1} \dot{\bar{R}} \int_{\bar{\Sigma}} \overline{\mathbf{y}} \bullet \overline{\mathbf{n}}(\overline{\mathbf{y}}) \, G(\overline{\mathbf{x}} - \overline{\mathbf{y}}) \, d\bar{\Sigma}(\overline{\mathbf{y}})$$
$$- \varepsilon \bar{R}^{-2} \dot{\bar{R}} \, \overline{\mathbf{x}} \bullet \overline{\mathbf{n}}(\overline{\mathbf{x}}) \tag{23}$$

where $\bar{T}^{\infty} = R \, T^{\infty}$ and $\dot{\bar{R}} = d\bar{R}/d\bar{t}$. Eqs. (22) and (23) uniquely determine $\bar{V}$ and either $\bar{T}^{\infty}$, if the flux J is prescribed, or $\dot{\bar{R}}$ and J if the far-field temperature T^{∞} is prescribed.

If J is given, then $\bar{R}$ is the solution to the following equation:

$$\frac{d}{d\bar{t}} \log(\bar{R}(\bar{t})) = \bar{J}, \tag{24}$$

where $\bar{J} = J/(3/4\pi)\text{Vol}(\bar{\Omega}_1)$. If J is constant, then so is $\bar{J}$ since the $\text{Vol}(\bar{\Omega}_1)$ does not change in time. Note the difference between J and $\bar{J}$ is of second order in the perturbation size. When J is constant, the solution to Eq. (24), with $\bar{R}(0) = 1$, is

$$\bar{R}(\bar{t}) = \exp(\bar{J}\,\bar{t}) \tag{25}$$

and the time scales t and $\bar{t}$ are related by

$$t = \frac{1}{3\bar{J}}(\exp(3\bar{J}\,\bar{t}) - 1). \tag{26}$$

Note that to leading order in the perturbation size, Eqs. (25)–(26) reduce to the result of linear theory given in Eq. (13).

3.2. Numerical implementation

The boundary integral method used in this work will be described only briefly here. Additional implementation details may be found elsewhere [10]. The interface $\bar{\Sigma}$ is discretized using an adaptive unstructured mesh of flat triangles [27], with N marker points (triangle vertices). The integrals in Eqs. (22) and (23) are discretized using trapezoid-rule integration, with the caveat that for triangles in Eq. (23), where the point of evaluation $\mathbf{x}$ lies on the triangle over which the integration in $\mathbf{y}$ is performed, another more accurate technique is used. This is necessary because for these triangles, the integrand is singular since $G(\mathbf{x} - \mathbf{y}) = 1/4\pi|\mathbf{x} - \mathbf{y}|$. To remove the singularity, we use a grid-mapping technique based on Duffy's transformation [10, 23]. The normal velocity $\bar{V}$ is obtained by solving the discretized version of Eqs. (22) and (23) iteratively using the solver GMRES [24]. The normal vector and curvature are obtained using a local parabolic surface fitting algorithm [25].

The marker point positions are evolved using an explicit second order accurate Runge–Kutta time stepping method. There is a time step restriction $\Delta t \sim h^{3/2}$ for stability [10] where h is the smallest edge length on the triangulated mesh.

At each time step of the simulation, the surface triangulation of $\bar{\Sigma}$ is restructured using the adaptive algorithm developed in Refs. [26,27]. The algorithm is based on local remeshing techniques that include dynamic displacement of marker points on the surface, marker-point reconnection, addition and subtraction. The resulting discretization is fully unstructured and minimizes a mesh energy function. The minimum occurs when the mesh resolves the local length scales to a prescribed accuracy. Here, the local length scale to be resolved is determined by the radius of curvature so that marker points are clustered in regions of high curvature (in absolute value). Correspondingly, the local edge-length of a triangle is $h \sim N_0^{-1/2}|\bar{\kappa}_{\max}|^{-1}$ where $|\bar{\kappa}_{\max}|$ is a measure of the local curvatures (see Ref. [27] for details). The parameter N_0 is the number of marker points used to discretize a spherical crystal and sets the accuracy of the simulation (the error is proportional to N_0^{-1}).

The adaptive remeshing algorithm makes the simulations efficient because the total number of marker points N used to discretize $\bar{\Sigma}$ at a time $\bar{t}$ is minimized and is a function of the instantaneous shape only (the volume change of the crystal has been scaled out of the simulation). Dynamic displacement and reconnection of marker points result in nearly equilateral triangles that minimize errors in the surface representation and numerical integration techniques. As a result, long-time simulations of complex three-dimensional crystal morphologies are feasible and accurate.

4. Comparison between theory and numerical simulations

4.1. Self-similar evolution

We compare the growth of a single spherical harmonic perturbation of a sphere under the conditions of constant undercooling T^{∞} and constant flux J. In the latter case, when $J = J_l$, where l is the polar perturbation wavenumber, self-similar growth is predicted by the linear theory in Section 2.2 and in Ref. [1]. To estimate the perturbation size in the nonlinear simulation, relative to an equivalent sphere[5], we take

$$\bar{\delta} = \max_{\bar{\Sigma}}|\overline{r_{\Sigma}} - 1|, \tag{27}$$

since the overall bulk growth is scaled out of the evolution through $R(t)$. Note that for the linear solution, we take the perturbation

$$\bar{\delta} = \max_{\theta,\phi} \sum_{l,m} \frac{\delta_{l,m}(t(\bar{t}))}{\bar{R}}|Y_{l,m}(\theta,\phi)|.$$

In Fig. 1 (upper), the evolution of $\bar{\delta}$ is shown as a function of $\bar{R}$ for several values of the initial perturbation amplitude $\delta_{l,m}(0) = 0.1$, 0.2 and 0.4 with $l = 4$, $m = 0$ and $\varepsilon = 0.1$ under constant flux conditions for several values of flux. The simulations are performed using $N_0 = 362$ which sets the accuracy as described in Section 3.2. The actual number of points used at time $\bar{t} = 0$ in the

---

[5] The equivalent sphere of a domain is defined as the sphere containing the same volume as the domain; the equivalent radius is defined as the radius of the equivalent sphere.
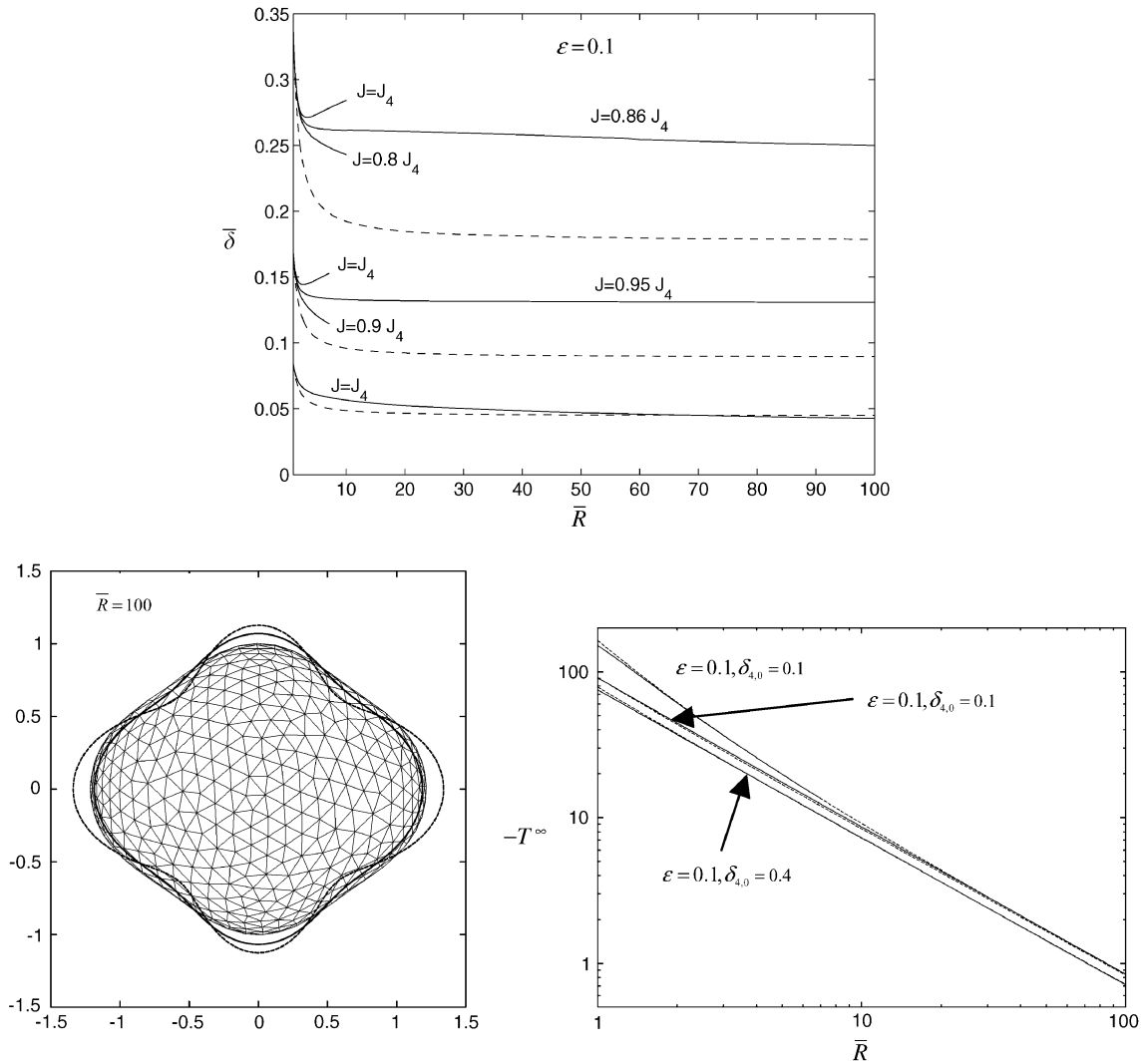
Fig. 1. The effect of nonlinearity on the critical flux for asymptotic self-similar growth. The evolution of the perturbation is shown for several initial amplitudes and fluxes. Solid: nonlinear simulations; dashed: linear theory with $J = J_4$. The crystal morphologies (surface mesh) at the final radius $\bar{R} = 100$ are shown for $\delta_{4,0} = 0.4$ on the lower left (viewed from the positive y-axis). Dashed: slice of the initial condition; solid: slice of the limiting (self-similar) linear solution. On the lower right: the (unscaled) undercooling to maintain constant flux conditions for self-similar growth.

simulations is $N = 362$ ($\delta_{4,0}(0) = 0.1$), 503 ($\delta_{4,0}(0) = 0.2$) and 836 ($\delta_{4,0}(0) = 0.4$). At later times, N slightly decreases since there is some decay of the perturbations. We have determined that at these resolutions, the nonlinear solutions are highly accurate.

The dashed and solid lines, in Fig. 1 (upper and lower right), correspond to the linear and nonlinear solutions, respectively. There is very good

agreement between the theory and simulation for the smallest initial perturbation $\delta_{4,0}(0) = 0.1$. For the other perturbations, nonlinearity plays an important role. For example, taking the (unscaled) flux $J = J_4$ in the nonlinear simulations with $\delta_{4,0}(0) = 0.2$ and 0.4 results in the growth of the perturbation. When the flux $J \ll J_4$, perturbations decay. Thus, assuming the results depend continuously upon J, we conclude that there exists a

nonlinear critical flux $J_{l,\mathrm{NL}}$ for which non linear self-similar growth is achieved. We note that in 2D we have been able to demonstrate the existence of a nonlinear critical flux by directly solving the equations governing self-similar evolution [18]. An extension of this 2D work to solve the self-similar equations in 3D is currently underway. The results of our 3D simulations in Fig. 1 (upper) suggest that for $\delta_{4,0}(0) = 0.2$ we have $J_{4,\mathrm{NL}} \approx 0.95\, J_4$ while for $\delta_{4,0}(0) = 0.4$ we obtain $J_{4,NL} \approx 0.86\, J_4$. Note that the deviation from linear theory is at the second order in the perturbation size as expected.

In Fig. 1 (lower left), the morphologies of the crystals corresponding to $\delta_{4,0}(0) = 0.4$ and $J \approx 0.86\, J_4$ are shown; the view is from the positive y-axis. The dashed and solid curves denote the boundaries of the initial condition and linear solution, in the $\bar{R} \to \infty$ limit, respectively. The surface triangulation is the nonlinear crystal surface at $\bar{R} = 100$. Although the initial condition and the limiting linear solution have regions of negative curvature, the nonlinear self-similar shapes have positive curvature. We note that in 2D, we have calculated nonlinear, self-similar growing morphologies with negative curvature [18].

In Fig. 1 (lower right), the (unscaled) far-field temperature T^∞ is shown as a function of effective radius for the simulations shown in Fig. 1 (upper). We also include a case in which $\varepsilon = 1.0$[6]. The dashed lines are the result of linear theory, given explicitly in terms of (un-scaled) time t from Eq. (11) as

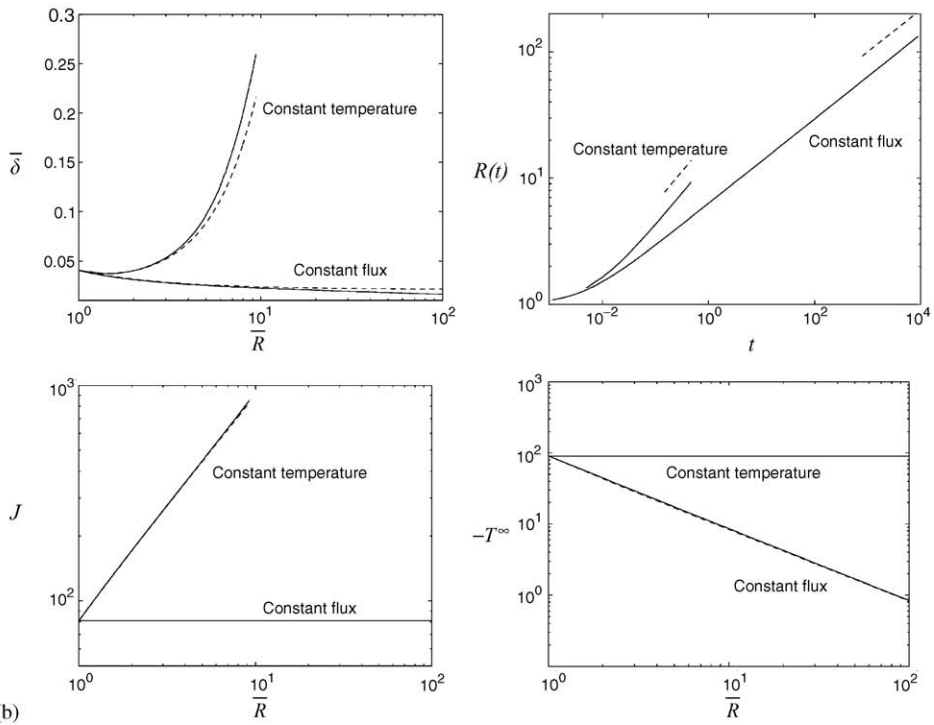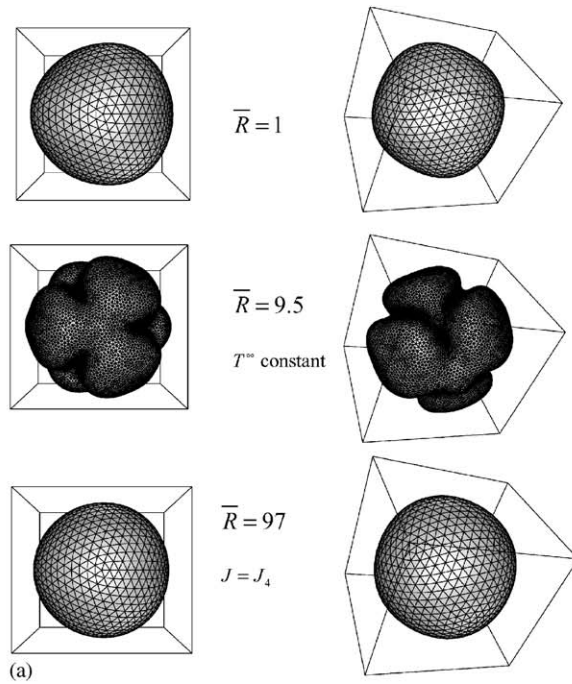$$T^\infty(t) = -\frac{2 + J\left(1 + \varepsilon/(1+3Jt)^{1/3}\right)}{(1+3Jt)^{1/3}} \tag{28}$$

and the solid lines are the result of the nonlinear simulations. There is very good agreement between the theory and simulations. The undercooling is insensitive to nonlinearity and is well approximated by formula (28) because temperature perturbations arising from shape variation decay rapidly with the distance from the crystal. This suggests that it is possible to achieve constant flux

conditions in an experiment by imposing Eq. (28) which does not require feedback of the size of the growing crystal. In order to simulate self-similar conditions, the flux $J = J_l$, or for more accurate results $J = J_{l,\mathrm{NL}}$, should be used.

In Fig. 2(a), the crystal morphologies resulting from an initial perturbation $r_\Sigma(\theta, \phi, 0) = 1 + 0.1\, Y_{4,3}(\theta, \phi)$ are shown for constant flux $J = J_4$ and for constant undercooling T^∞ such that the initial flux is $J(t=0) = J_4$. The kinetic parameter is $\varepsilon = 0.1$. Under constant flux conditions (bottom), the Mullins–Sekerka instability is suppressed and the crystal evolves to an asymptotically self-similar shape as predicted by linear theory in Section 2.2 and in Ref. [1]. As predicted by linear theory, the non-zero azimuthal wavenumber ($m = 3$) does not affect the result. Under constant undercooling (middle), the instability and growth of the perturbation is evident. In Fig. 2(b), further details of the simulations are shown. In the upper left graph, the nonlinear perturbations (solid) are shown together with their linear counter-parts (dashed). The growth of the equivalent radii is as predicted by linear theory (upper right graph). The asymptotic behaviors $t^{1/2}$, for constant T^∞, and $t^{1/3}$ for constant flux are shown (dashed curves). In the lower graphs, the evolution of the flux and under-cooling are shown for the two cases. In both, the solid curves, which denote the result of nonlinear simulations, and the dashed curves, which are the result of the linear analysis, overlap. These figures show that both the far-field temperature and flux are well-approximated by formula (11).

Next, we examine the role of the axial wave-number l on nonlinear self-similar evolution. In Fig. 3(a) and (b), we show the evolution of a high-mode initial perturbation $r_\Sigma(\theta, \phi, 0) = 1 + 0.1\, Y_{10,6}(\theta, \phi)$. The kinetic parameter is $\varepsilon = 0.25$. Since we find that the linear flux J_{10} is super-critical due to nonlinearity, we present results using a reduced flux $J = 0.85 J_{10}$. This yields nearly self-similar growth up to a radius of approximately 7. After this initial evolution, instability of the lower modes becomes visible. The low modes are produced through nonlinearity (numerical error does not play a role as evidenced by the grid refinement study) and eventually dominate the shape as seen in Fig. 3(b). The flux
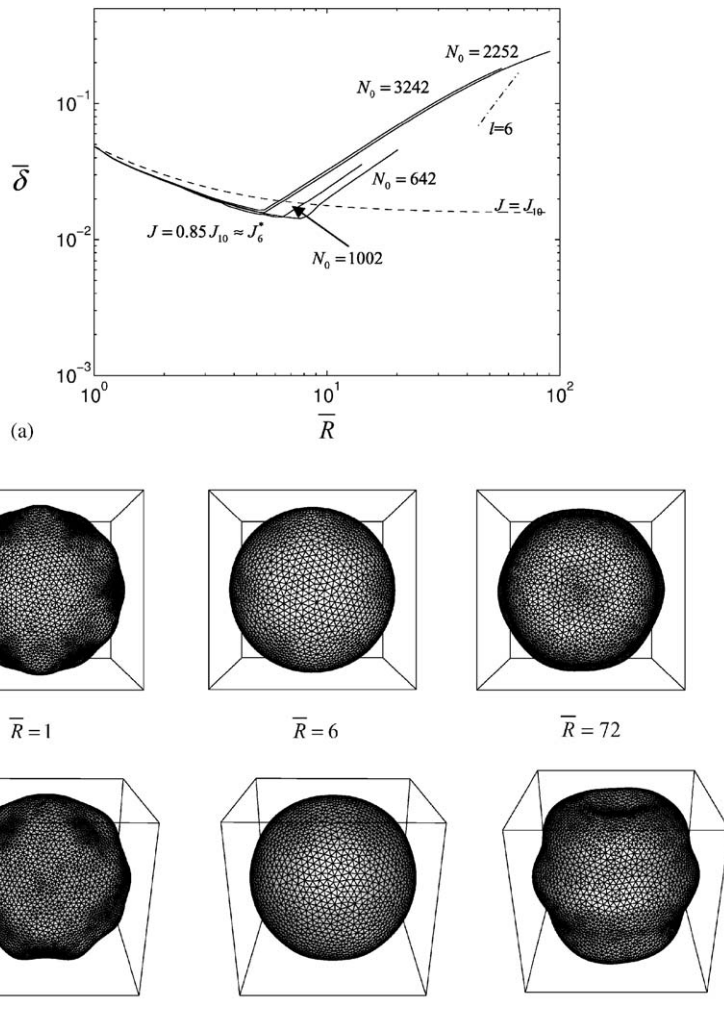
---

[6] We find that, in general, perturbations decay more rapidly as the kinetics increases (consistent with linear theory) and correspondingly, there is better agreement between linear theory and nonlinear simulations.

(a)

(b)

(a)

(b)

Fig. 3. (a). Deviation from self-similar growth due to the nonlinear creation of unstable modes for a high-mode initial perturbation $r_\Sigma = 1 + 0.1 \; Y_{10,6}(\theta, \phi)$. Solid: nonlinear perturbation $\bar{\delta}$ under labeled conditions. dashed: linear theory; dot–dashed: asymptotic growth rate from linear theory assuming $l = 6$ is the fastest growing mode. (b). The morphologies corresponding to the simulation in Fig. 3(a) with $J = 0.85 \; J_{10}$ and $N_0 = 2252$. The actual number of points initially is $N = 6,400$ and is approximately $N = 5000$ at the final radius shown. In between, the number of points varies non-monotonically consistent with the perturbation evolution. View from the positive z-axis (top), a three-dimensional view (bottom). Left column: initial condition; middle and right columns: before and after unstable low-modes affect the shape.

Fig. 2. (a). Crystal morphologies corresponding to unstable growth under constant undercooling T^∞ (middle) and to asymptotically self-similar growth under the constant flux $J = J_4$ (bottom) from the initial condition $r_\Sigma = 1 + 0.1 \; Y_{4,3}(\theta, \phi)$ (top). Left: view from the positive z-axis ($\theta = 0$); right: a three-dimensional view. The number of points is $N_0 = 1002$. In the case of constant flux, the actual number of points is $N \approx N_0$. In the case of constant temperature, N increases to approximately 18,600 by the end of the simulation. (b) Comparison of linear theory (dashed) and nonlinear simulations (solid) for quantities from the two simulations in Fig. 2(a). Upper left: evolution of the perturbation amplitude $\bar{\delta}$; Upper right: Evolution of the equivalent radius as a function of (unscaled) time (recall $\bar{R}(\bar{t}) = R(t(\bar{t}))$); the asymptotic slopes from linear theory are also shown. bottom left: evolution of flux; bottom right: evolution of (unscaled) far-field temperature.

$J = 0.85 \ J_{10} \approx J_6^*$ is the flux that makes the $l = 6$ mode to be the fastest growing spherical harmonic according to linear theory. The corresponding linear growth of an $l = 6$ mode is shown as the dot-dashed curve in Fig. 3(a). The final shape ($\bar{R} = 72$) in Fig. 3(b) seems to confirm the dominance of the $l = 6$ mode as a 6-fold morphology is clearly distinguishable. This simulation suggests that self-similar evolution is more difficult to maintain for high mode perturbations because lower modes are created by nonlinearity and subsequently grow and affect the shape evolution. Indeed, we observe a similar phenomenon with polar modes $l = 6$ and 5 where the $l = 4$ and 3 respectively become dominant.

The simulation for $l = 10$ in Fig. 3 also suggests that it should be easier to control the shape of a growing crystal by evolving the crystal using the flux $J = J_l^*$ to make an l-mode spherical harmonic dominate the shape rather than by evolving an initial l-mode spherical harmonic self-similarly using $J = J_l$ since the latter method works for a limited range of crystal sizes if l is large. We investigate this idea in the next section.

4.2. Controlling the crystal morphology using $J=J_l^*$

We now consider evolution of a crystal from a multi-mode initial perturbation $r_\Sigma(\theta, \phi, 0) = 1 + 0.1 \left(Y_{4,0}(\theta, \phi) + Y_{5,2}(\theta, \phi) + Y_{6,2}(\theta, \phi) + Y_{10,6}(\theta, \phi) \right)$ where we wish to make mode $l = 5$ dominate the evolving shape. Linear theory, as discussed in Section 2.2, predicts that this can be achieved by taking the constant flux $J = J_5^*$ during growth (see Eq. (15)). In fact with $J = J_5^*$, all modes up to and including $l = 7$ also grow (as can be seen from Eq. (14)). We find that there is a correction to this flux due to nonlinearity. In Fig. 4(a), the nonlinear evolution of the multimode initial condition is shown with the slightly reduced flux $J = 0.9 J_5^*$ and interface kinetics $\varepsilon = 0.1$. As predicted by the theory, the crystal strikingly evolves to a 5-fold shape although the evolution is quite different from that predicted by linear theory as seen in Fig. 4 (b,left) where the perturbation amplitudes are shown for the nonlinear simulation (solid) and linear theory (dashed). At early times, nonlinearity enhances the perturbation compared to that

determined by linear theory. At later times, nonlinearity is strongly stabilizing; the mode $l = 5$ stabilizes at approximately $\bar{R} = 15$. Further growth and stabilization of the perturbation for $\bar{R} > 15$ is associated to the development of the bulb in the center of crystal that is clearly visible when $\bar{R} = 118$. Linear theory predicts a much more rapid growth of the perturbation. In fact, according to linear theory, the interface self-intersects at a finite time. This does not occur for the nonlinear solution. Very interestingly, the far-field temperature in the nonlinear simulation (solid) is well predicted by the formula (11), shown as dashed, as seen in Fig. 4 (b,right). This result strongly suggests that it is possible to control the shape of evolving crystals well into the nonlinear regime.

We note that had the polar mode $l = 5$ not been present in the initial perturbed shape, this mode would have been generated by nonlinearity (as seen in Fig. 3(a) for mode $l = 6$) and would eventually have dominated the shape because of the imposed flux conditions.

5. Discussion and future directions

We extended our previous analysis of the linear evolution of non-spherical growing crystals in three dimensions into the nonlinear regime. We focussed on a solid crystal growing in an undercooled liquid with isotropic surface tension and interface kinetics. We used a new, adaptive boundary integral method to simulate the morphological evolution of the growing crystals. We found that when the far-field heat flux into the system is prescribed by appropriately varying the undercooling in the far-field, the Mullins–Sekerka instability that would arise under constant undercooling can be suppressed. In particular, we demonstrated that there exist critical conditions of flux at which self-similar or nearly self-similar nonlinear evolution occurs and the shape is dominated by a given mode leading to non-spherical, nearly shape invariant growing crystals. We provided a simulation of a physical experiment that might be able to be carried out in a laboratory in which a desired shape of a crystal is achieved
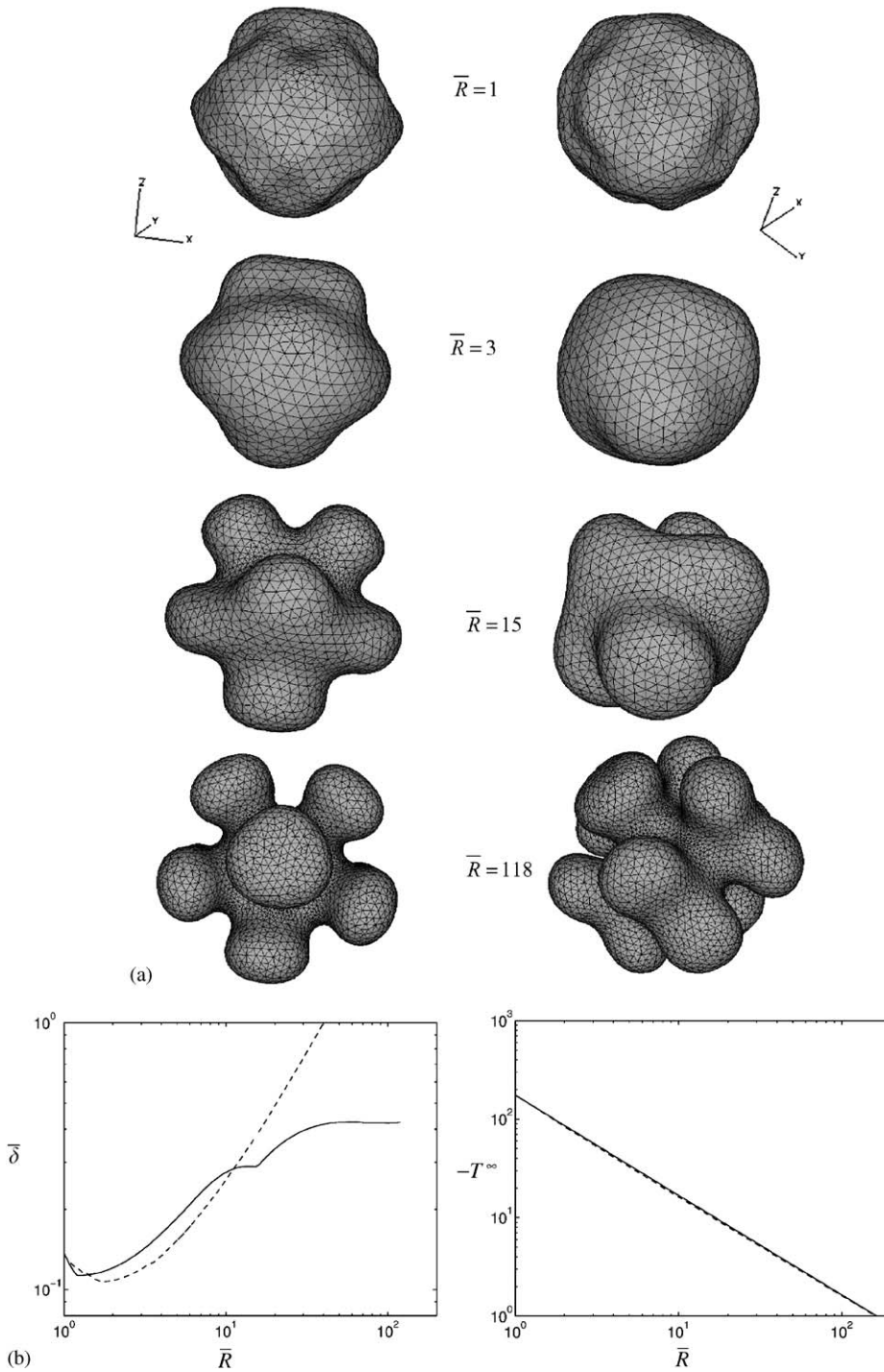
Fig. 4. (a). Shape control using the reduced flux $J = 0.9J_5^*$. The appearance of mode l = 5 is evident. The number of points $N_0 = 1002$ with $N = 1100$ initially and 6158 at the final radius shown. (b). Left: growth of the perturbation in Fig. 4(a). Solid: nonlinear simulation; dashed: linear theory. Right: evolution of the (unscaled) undercooling.
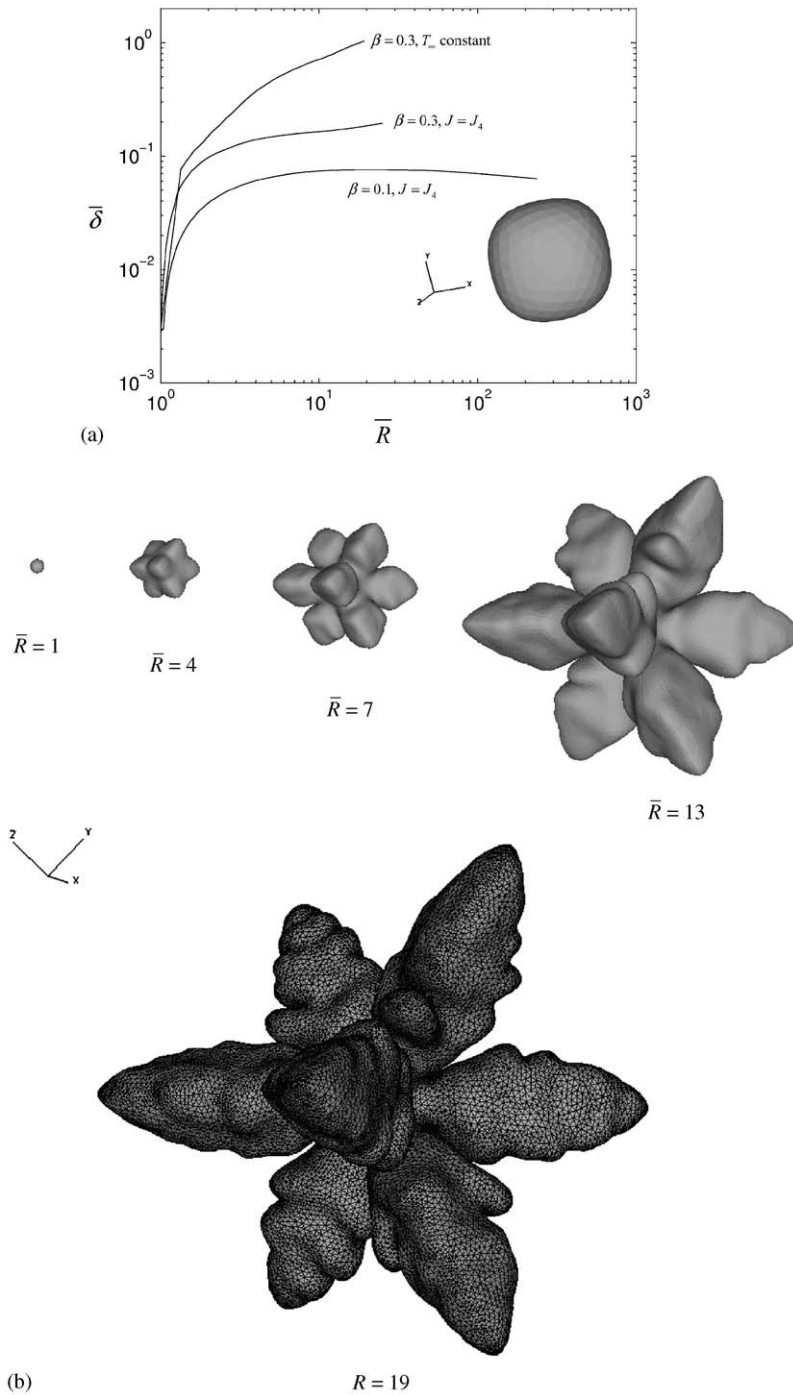
(a)

$\bar{R} = 1$

$\bar{R} = 4$

$\bar{R} = 7$

$\bar{R} = 13$

(b)

$R = 19$

Fig. 5. (a). The perturbation evolution with kinetic anisotropy. Inset: the nearly self-similar configuration for $\beta = 0.1$ is shown ($N = N_0 = 362$). (b). The morphologies during unstable evolution with constant far-field temperature and kinetic anisotropy corresponding to the case $\beta = 0.3$ in (a). The number of points $N = N_0 = 362$ initially and N increases to 23,261 at the final radius shown.

and maintained during growth by appropriately prescribing the far-field heat flux.

Several physical effects may be important and were neglected in the present analysis. These include the anisotropy of the crystal, crystal/crystal interactions, solute and elastic effects and flow. Studies of these effects are underway. For example, crystal/crystal interactions are expected to result in decreased instability by decreasing the undercooling of the individual crystals. Our preliminary results [28] indicate that anisotropy may also reduce instability. In a subsequent work, we demonstrate that self-similarly evolving anisotropic crystals exist and the associated critical fluxes are lower than those for the isotropic case [18,28]. Because the critical flux is lower, shape perturbations have more chance to grow in the isotropic case than in the anisotropic case and in this sense, the anisotropic evolution is more stable. Of course, this also means that if one applies the isotropic flux in the presence of anisotropy, unstable evolution will typically result. In Fig. 5 we present the evolution of a crystal with 4-fold kinetic anisotropy

$$\varepsilon = \varepsilon_0 \left(1 - \beta \left(3 - 4 \left(n_1^4 + n_2^4 + n_3^4 \right) \right) \right)$$

where n_i denotes the components of the normal and β is the anisotropy coefficient. We take $\varepsilon_0 = 0.1$ and $\beta = 0.1$ and 0.3. Under constant undercooling with $\beta = 0.3$, the perturbation grows (as seen in Fig. 5(a)) and the shape becomes complex and dendritic as seen in Fig. 5(b). The adaptive mesh is shown in the last frame. Under constant flux conditions $J = J_4$ with $\beta = 0.3$, the perturbation grows (Fig. 5(a)) since the isotropic critical flux is larger than that for the anisotropic case (the anisotropic critical flux is a decreasing function of the kinetic anisotropy parameter β [18,28]) . When β is reduced to 0.1 the critical fluxes for the isotropic and anisotropic cases are nearly equal and so the perturbation grows nearly self-similarly. The morphology for $\beta = 0.1$ is shown in the inset in Fig. 5(a).

Acknowledgements

References

[1] V. Cristini, J. Lowengrub, J. Crystal Growth 240 (2002) 267.
[2] W. Mullins, R. Sekerka, J. Appl. Phys. 34 (1963) 323.
[3] S.R. Coriell, R.L. Parker, J. Appl. Phys. 36 (1965) 632.
[4] S.R. Coriell, R.L. Parker, in: H.S. Peiser (Ed.), Crystal Growth, Pergamon Press, Oxford, 1967, p. 703.
[5] L.N. Brush, R.F. Sekerka, J. Crystal Growth 96 (1989) 419.
[6] P.W. Voorhees, Ann. Rev. Mater. Sci. 22 (1992) 197.
[7] M.E. Glicksman, R.N. Smith, S.P. Marsh, R. Kuklinski, Metter. Trans. A—Phys. Metter. Mat. Sci. 23 (1992) 659.
[8] M.E. Glicksman, L.M. Mizenko, M.E. Rettenmayer, S.P. Marsh, Mater. Sci. Eng. A—Struct. Mater. Props. Microstruc. Process. 178 (1994) 137.
[9] S. Marsh. Kinetics of diffusion-limited microstructural coarsening, Ph.D. Thesis, Rensselaer Polytechnic Institute, 1989; L. Meloro, Evolution of microstructures in tin–bismuth alloys, M.S. Thesis, Rensselaer Polytechnic Institute, 1988.
[10] X. Li, J.S. Lowengrub, Q. Nie, V. Cristini, P. Leo, Mett. Mater. Trans. A 34A (2003) 1421.
[11] M. Thompson, P. Voorhees, Acta Mater. 47 (1999) 983.
[12] R. Mueller, D. Gross, Comput. Mater. Sci. 11 (1998) 35.
[13] R. Mueller, D. Gross, Comput. Mater. Sci. 16 (1999) 53.
[14] L.Q. Chen, Ann. Rev. Mater. Res. 32 (2003) 113.
[15] W.J. Boettinger, J.A. Warren, C. Beckermann, A. Karma, Ann. Rev. Mater. Res. 32 (2002) 163.
[16] A. Schmidt, J. Comp. Phys. 125 (1996) 293.
[17] F. Gibou, R. Fedkiw, R. Caflisch, S. Osher, SIAM J. Sci. Comput. 19 (2003) 183.
[18] S. Li, J.S. Lowengrub, V. Cristini, P.H.Leo, J. Crystal Growth , in press.
[19] M.E. Glicksman, R.J. Schaefer, J.D. Ayers, Metal. Trans. A 7A (1976) 1749.
[20] M.E. Glicksman, 2003, private communication;; H. Singer, 2003, private communication.
[21] O.D. Kellogg, Foundations of Potential Theory, Springer, Berlin, 1929.
[22] J. Zhu, X. Chen, T.Y. Hou, J. Comp. Phys. 127 (1996) 246.

[23] K.E. Atkinson, The Numerical Solution of Integral Equations of the Second Kind, Cambridge University Press, Cambridge, 1997.

[24] Y. Saad, M.R. Schultz, SIAM J. Sci. Statist. Comput. 7 (1986) 856.

[25] A.Z. Zinchenko, M.A. Rother, R.H. Davis, Phys. Fluids 9 (1977) 1493.

[26] V. Cristini, J. Blawzdziewcz, M. Loewenberg, Phys. Fluids 10 (1998) 1781.

[27] V. Cristini, J. Blawzdziewcz, M. Loewenberg, J. Comp. Phys. 168 (2001) 445.

[28] S. Li, Morphological control of crystal growth, Ph.D. Thesis, University of Minnesota, (degree expected 2005).